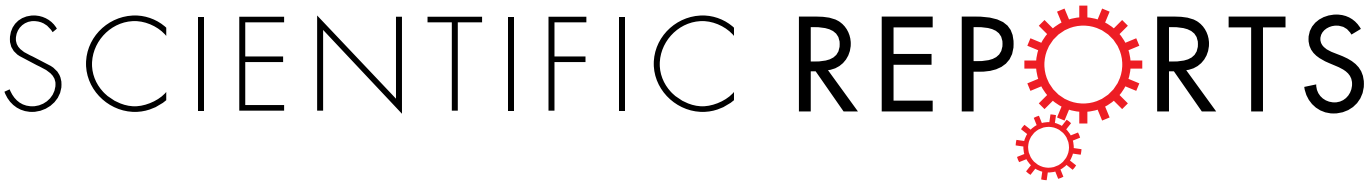

OPEN

Effective-mass model and magneto-optical properties in hybrid perovskites

Received: 12 April 2016
Accepted: 06 June 2016
Published: 24 June 2016

Z. G. Yu

Hybrid inorganic-organic perovskites have proven to be a revolutionary material for low-cost photovoltaic applications. They also exhibit many other interesting properties, including giant Rashba splitting, large-radius Wannier excitons, and novel magneto-optical effects. Understanding these properties as well as the detailed mechanism of photovoltaics requires a reliable and accessible electronic structure, on which models of transport, excitonic, and magneto-optical properties can be efficiently developed. Here we construct an effective-mass model for the hybrid perovskites based on the group theory, experiment, and first-principles calculations. Using this model, we relate the Rashba splitting with the inversion-asymmetry parameter in the tetragonal perovskites, evaluate anisotropic *g*-factors for both conduction and valence bands, and elucidate the magnetic-field effect on photoluminescence and its dependence on the intensity of photoexcitation. The diamagnetic effect of exciton is calculated for an arbitrarily strong magnetic field. The pronounced excitonic peak emerged at intermediate magnetic fields in cyclotron resonance is assigned to the $3D_{\pm 2}$ states, whose splitting can be used to estimate the difference in the effective masses of electron and hole.

Hybrid organic-inorganic perovskites such as $CH_3NH_3PbI_3$ represents a revolutionary breakthrough for low-cost solar cells[1–4] because of their desirable optical and carrier transport properties[5,6]. The materials also exhibit many intriguing features, including strong spin-orbit coupling[7] and the associated Rashba effect[8,9], large-radius Wannier excitons[10], and novel magnetic-field effect (MFE) in photoluminescence (PL) and photoconduction[11,12], and show promise in light-emitting[13] and thermoelectric[14] applications.

These outstanding properties are interconnected and are ultimately determined by the material's unusual electronic structure, which has been intensively studied by a variety of density-functional calculations[15–17]. While such first-principles calculations are indispensable in predicting the crystal structure, carrier effective mass, and band gap, they become increasingly unwieldy in studying processes involving excited states and under external fields. An alternative is to develop an effective-mass Hamiltonian[18–20], which is both tractable and transparent in physics with parameters determined by experimentally measured properties. These properties, such as effective masses and *g*-factors, are usually obtained from magneto-optical studies, which turn out to be a major experimental means of validating the principle of the band theory of semiconductors.

Exciton, an electron-hole pair bounded by the Coulomb interaction, is a fundamental excitation in semiconductors. The exciton binding energy in the hybrid perovskites is critical to photovoltaic and light-emitting efficiencies and has been a subject of intense debate[21,22]. This controversy can be resolved via a definitive measurement of magneto-optical absorption (cyclotron resonance)[23], which reveals characters of exciton as well as constituent electron and hole. To take advantage of the wealth of information, a detailed analysis of cyclotron resonance is needed. While diamagnetic response of an exciton is similar to that of a hydrogen, a key difference is that the electron and hole in an exciton have a comparable effective mass, particularly in the hybrid perovskites.

A moderate magnetic field less than 1 T is found to be able to influence exciton PL in $CH_3NH_3PbI_3$[11,12], indicating that magnetic field is a versatile tool for studying excitons and free carriers. This MFE has been attributed to the Δg (the difference between electron and hole *g*-factors) mechanism, frequently encountered in organic radical pairs[24]. However, the lack of knowledge on the *g*-factors in $CH_3NH_3PbI_3$ hampers the development of a clear understanding of the MFE. In addition, the MFE is sensitive to the intensity of photoexcitation[12], which is not well understood.

ISP/Applied Sciences Laboratory, Washington State University, Spokane, Washington 99210, USA. Correspondence and requests for materials should be addressed to Z.G.Y. (email: zhigang.yu@yahoo.com or zhi-gang.yu@wsu.edu)

Here we construct an effective-mass model of $CH_3NH_3PbI_3$ based on information available in literature. This model, which can be extended to other hybrid perovskites by using suitable parameters, reveals connections among the *g*-factors, effective masses, and Rashba spin splittings. Using this model, we examine the MFE on exciton PL and find that the MFE is controlled by the interplay of exchange energy, exciton (spin) relaxation time, and the Zeeman energy. Besides the Δg mechanism, a Σg (summation of the electron and hole *g*-factors) mechanism can manifest itself in the MFE. The dependence of MFE on the intensity of photoexcitations is quantitatively explained in terms of the screening effect by the photogenerated carriers, which greatly reduces the exchange coupling of excitons. The diamagnetic effect on excitons under an arbitrarily large magnetic field is reliably calculated and in an excellent agreement with recent cyclotron measurements. The experimentally observed pronounced excitonic absorption peak, induced by the magnetic-field, can be attributed to the $3D_{\pm 2}$ states, whose energy splitting can be used to determine the difference in electron and hole effective masses. Our results demonstrate the efficacy of the effective-mass model in understanding magneto-optical properties and suggest it a foundation for systematically studying many other transport, optical, and spintronic processes in the hybrid perovskites.

Results

Model. Crystalline $CH_3NH_3PbI_3$ can have the high-temperature α-phase with the pseudo cubic (O_h) symmetry, the intermediate-temperature β-phase with the tetragonal (C_{4v}) symmetry, and the low-temperature orthorhombic γ phase. Phase transitions from high to low temperatures, being of group-subgroup type, take place at 333 K and 150 K, respectively[25,26]. We focus in this paper on the β-phase, which is also a good description of the approximately uniaxial γ-phase[25]. In the β-phase, PbI_6 octahedra are misalign with the C-axis (symmetry axis of C_{4v}), and the structure is noncentrosymmetric.

First-principle calculations indicate that the valence and conduction bands are mainly associated with cationic (Pb) *s* and *p* orbitals, respectively[15–17,27], denoted as *S*, *X*, *Y*, and *Z*. The direct band gap is located at *R* point[7], which has the same C_{4v} symmetry as the crystal structure. Since physically relevant states are those close to the band extremes, we derive band structure in the neighborhood of *R* point, via the $\boldsymbol{k}\cdot\boldsymbol{p}$ method, where $\boldsymbol{k}$ is the wave vector away from the *R* point. In this method, the wave function at $\boldsymbol{k}$ is expressed as $\psi_{n\boldsymbol{k}} = e^{i\boldsymbol{k}\cdot\boldsymbol{r}}u_n(\boldsymbol{r})$ with $u_n(\boldsymbol{r})$ being the basis function of *n*th band at the *R* point. We note that the $\boldsymbol{k}\cdot\boldsymbol{p}$ Hamiltonian for zinc-blende semiconductors is not suitable for the tetragonal perovskites[15]. In the absence of magnetic field, the Hamiltonian can be written as $H = H_0 + H_{SO}$, where $H_0 = p^2/2\,m + V(\boldsymbol{r})$ is spin-independent part and $H_{SO} = \frac{\hbar}{4m^2c^2}\nabla V \times \boldsymbol{p}\cdot\boldsymbol{\sigma}$ is the spin-orbit coupling (SOC). Here $V(\boldsymbol{r})$ is periodic potential, $\boldsymbol{p}$ is momentum, *m* is free electron mass, *c* is the speed of light, and $\boldsymbol{\sigma}$ are the Pauli matrices.

In the β-phase, the potential should be an identical representation of group C_{4v}, a subgroup of the cubic group O_h, and therefore can be expressed in terms of the O_h representations, in particular, its first three irreducible representations, $\Gamma_1 \oplus \Gamma_{12} \oplus \Gamma_{15}$. Neglecting the trivial Γ_1 representation, we write $V(\boldsymbol{r}) = \sum_j c_j d_j$, where $d_1 = 2z^2 - x^2 - y^2$ and $d_2 = x^2 - y^2$ are the basis functions of Γ_{12}, and $d_3 = x$, $d_4 = y$, and $d_5 = z$ are the basis functions of Γ_{15}. By requiring $D(G_i)V(\boldsymbol{r}) = V(\boldsymbol{r})$ with G_i being the symmetry operators in C_{4v}, $c_2 = c_3 = c_4 = 0$. The nonzero c_1 reflects a crystal-field splitting between *Z* and *X* (*Y*), $\langle X|H_0|X\rangle = \langle Y|H_0|Y\rangle = -\langle Z|H_0|Z\rangle/2 = \delta/3$. And c_5 originates from the lack of inversion asymmetry in C_{4v}, giving rise to[28] $\langle S|H_0|Z\rangle = \langle Z|H_0|S\rangle^* = c_5\langle S|z|Z\rangle \equiv \zeta$.

The Hamiltonian H_0, up to the second order of *k*, can be written as[19,20]

$$H_0 = \frac{\hbar^2k^2}{2m} + \begin{pmatrix} E_v & iP_\perp k_x & iP_\perp k_y & iP_\parallel k_z + \zeta \\ -iP_\perp k_x & L_1k_x^2 + M_1k_y^2 + M_2k_z^2 + \frac{\delta}{3} & N_1k_xk_y & N_2k_xk_z \\ -iP_\perp k_y & N_1k_xk_y & M_1k_x^2 + L_1k_y^2 + M_2k_z^2 + \frac{\delta}{3} & N_3k_yk_z \\ -iP_\perp k_z + \zeta & N_2k_xk_z & N_3k_yk_z & M_3(k_x^2 + k_y^2) + L_2k_z^2 - \frac{2\delta}{3} \end{pmatrix}. \quad (1)$$

Here E_v is the valence-band maximum, L_i, M_i, and N_i are parameters due to the interaction between the conduction bands with far bands other than the valence band, and $P_\parallel = \frac{\hbar^2}{m}\langle S|\,-i\nabla|Z\rangle$ and $P_\perp = \frac{\hbar^2}{m}\langle S|\,-i\nabla|X\rangle = \frac{\hbar^2}{m}\langle S|\,-i\nabla|Y\rangle$ are the Kane parameters that connect the valence-band and conduction-band orbitals[20].

The SOC among the *p* orbitals mixes up and down spins, $\lambda = i\langle X\uparrow|H_{SO}|Y\downarrow\rangle = i\langle Y\uparrow|H_{SO}|Z\downarrow\rangle = i\langle Z\uparrow|H_{SO}|X\downarrow\rangle$, which is particularly strong in the hybrid perovskites due to the heavy element Pb, $\lambda = 1.2$–1.5 eV[7–9], and cannot be treated as a perturbation.

The crux of the $\boldsymbol{k}\cdot\boldsymbol{p}$ method is that the basis functions of $u_n(\boldsymbol{r})$ should be the eigenstates of *H* at $k = 0$[20], which can be achieved by choosing the following basis functions $u_n(\boldsymbol{r})$,

$$v_{+(-)} = S\uparrow(\downarrow), \quad (2)$$

$$c_{+(-)} = +(-)\frac{\cos\xi}{\sqrt{2}}[X - (+)iY]\uparrow(\downarrow) - \sin\xi Z\downarrow(\uparrow), \quad (3)$$

$$c'_{+(-)} = -(+)\frac{1}{\sqrt{2}}[X + (-)iY]\uparrow(\downarrow), \quad (4)$$

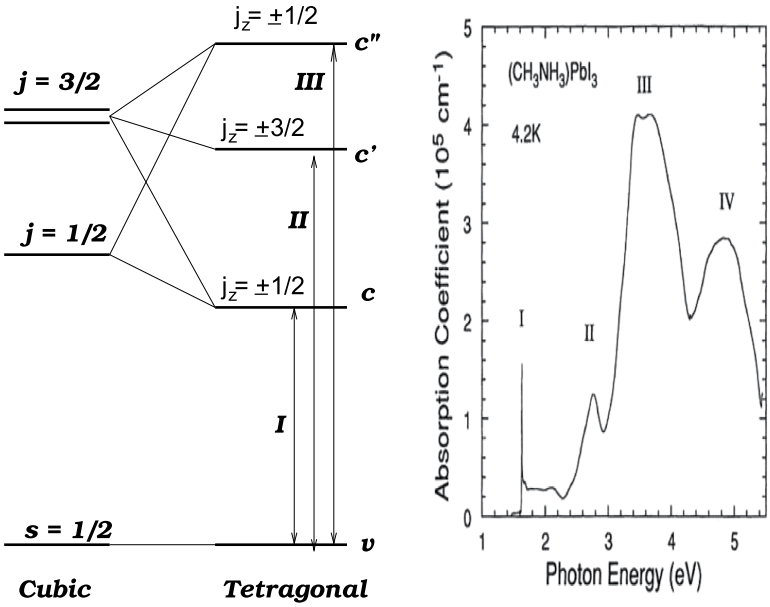

Figure 1. Schematic diagram of band edges and their angular momenta in $CH_3NH_3PbI_3$. The optical absorption spectrum is adapted from ref. 29.

$$c''_{+(-)} = +(-)\frac{\sin\xi}{\sqrt{2}}[X - (+)iY]\uparrow(\downarrow) + \cos\xi Z\downarrow(\uparrow), \tag{5}$$

with $\tan 2\xi = \frac{2\sqrt{2}\lambda}{\lambda - 3\delta}$. The angular momentum is $s = 1/2$ for the valence band $v_{\pm}$, and $j = 1/2$ ($\boldsymbol{j} = \boldsymbol{l} + \boldsymbol{s}$ with $l = 1$ and $s = 1/2$) for the first conduction band $c_{\pm}$. The two upper conduction bands, $c'_{\pm}$, and $c''_{\pm}$, have $j = 3/2$, with $j_z = \pm 3/2$ for $c'_{\pm}$ and $j_z = \pm 1/2$ for $c''_{\pm}$. The diagonal elements at $k = 0$ in these basis functions are E_v, $E_c = -\frac{1}{2}(\lambda + \delta) - \frac{1}{2}\sqrt{\lambda^2 + \delta^2 - 2\lambda\delta/3}$, $E_{c'} = 0$, $E_{c''} = -\frac{1}{2}(\lambda + \delta) + \frac{1}{2}\sqrt{\lambda^2 + \delta^2 - 2\lambda\delta/3}$. Here we temporally neglect ζ, which is small as compared to other parameters. In the measured absorption spectra of $CH_3NH_3PbI_3$ (Fig. 1), the first three peaks, located at 1.6 eV, 2.8 eV, and 3.4 eV[29], can be attributed to electron transitions from the valence band to the three conduction bands. Thus we obtain the values $E_v = -2.8$ eV, $E_c = -1.2$ eV, and $E_{c'} = 0.6$ eV, which fix the parameter values, $\lambda = 1.4$ eV, $\delta = -0.7$ eV, and $\sin\xi = 0.411$.

An applied magnetic field $\boldsymbol{B}$ have two effects on a charge carrier: paramagnetic magnetism due to the carrier's spin and diamagnetic orbital magnetism due to the lack of commutation among momentum components, $[k_\alpha, k_\beta] = -ie\epsilon_{\alpha\beta\gamma}B_\gamma/(\hbar c)$[30], where $\epsilon_{\alpha\beta\gamma}$ is the antisymmetric tensor of rank three. Because of the latter, the effective Zeeman energy of quasi-degenerate conduction-band orbitals can be written as

$$H_Z = -\frac{e}{2mc}(3\kappa_1 + 1)l_zB_z - \frac{e}{2mc}(3\kappa_2 + 1)(l_xB_x + l_yB_y) + \frac{e}{mc}\boldsymbol{s}\cdot\boldsymbol{B}, \tag{6}$$

where $\boldsymbol{l}$ ($l = 1$) is the angular momentum operator, and κ_1 and κ_2 are the Luttinger antisymmetric parameters for tetragonal structures.

The total Hamiltonian, in the presence of magnetic field $\boldsymbol{B}$, can now be written as

$$H = \frac{\hbar^2k^2}{2m} + \begin{pmatrix} H_A & H_B \\ H_B^+ & H_C \end{pmatrix}, \tag{7}$$

where 4×4 matrices H_A, H_B and H_C are displayed in the Methods section. In this Hamiltonian, we have eleven parameters, L_i and κ_i ($i = 1, 2$), M_i and N_i ($i = 1, 2, 3$), $P_{\|}$, and $P_{\perp}$. If the information at hand is insufficient to fix all these parameters, one can resort to the first principles calculations, or via the quasi-cubic symmetry, $L_1 = L_2$, $M_1 = M_2 = M_3$, and $\kappa_1 = \kappa_2$.

g-factors, effective masses, and cyclotron frequencies. The most important transport and optical processes occur in the conduction and valence bands, which are both nondegenerate (excluding spin). We map the above 8×8 Hamiltonian H_{mn} into two effective 2×2 Hamiltonians in spin space for these two bands by employing the Löwdin method for degenerate perturbation theory[31],

$$\widetilde{H}_{mn}(\boldsymbol{k}) = H_{mn}(\boldsymbol{k}) + \sum_l \frac{H_{ml}H_{ln}}{E_m(\boldsymbol{k}) - H_{ll}}. \tag{8}$$

Here $E_m(\boldsymbol{k})$ is the energy of mth band, which, for small $\boldsymbol{k}$, can be approximated by the band-edge value. Taking into account the non-commutative relations among $\boldsymbol{k}$ components, we obtain the effective Hamiltonians, up to the second order of k, for the valence and conduction bands, with basis functions of $v_\pm$ and $c_\pm$ in Eqs (2) and (3),

$$\widetilde{H}_{vv}(\boldsymbol{k}) = \widetilde{E}_v - \frac{\hbar k_\perp^2}{2m_{h\perp}} - \frac{\hbar k_z^2}{2m_{h\|}} + \alpha_{vr}(k_y\sigma_x - k_x\sigma_y) + \frac{\mu_B}{2}[g_{h\|}\sigma_z B_z + g_{h\perp}(\sigma_x B_x + \sigma_y B_y)], \tag{9}$$

$$\widetilde{H}_{cc}(\boldsymbol{k}) = \widetilde{E}_c + \frac{\hbar k_\perp^2}{2m_{e\perp}} + \frac{\hbar k_z^2}{2m_{e\|}} + \alpha_{vc}(k_y\sigma_x - k_x\sigma_y) + \frac{\mu_B}{2}[g_{e\|}\sigma_z B_z + g_{e\perp}(\sigma_x B_x + \sigma_y B_y)], \tag{10}$$

where $\mu_B \equiv e\hbar/(2\,mc)$ is the Bohr magneton, $\widetilde{E}_v \equiv E_v + \zeta^2\cos^2\xi/(E_v - E_{c''}) + \zeta^2\sin^2\xi/(E_v - E_c)$ and $\widetilde{E}_c \equiv E_c + \zeta^2\sin^2\xi/(E_c - E_v)$, which can be approximated by E_v and E_c.

The effective masses of valence band along and perpendicular to the C-axis in Eq. (9) are expressed as

$$\begin{aligned} -\frac{1}{m_{h\|}} &= \frac{1}{m} + \frac{2P_\|^2}{\hbar^2}\left(\frac{\cos^2\xi}{E_v - E_{c''}} + \frac{\sin^2\xi}{E_v - E_c}\right), \\ -\frac{1}{m_{h\perp}} &= \frac{1}{m} + \frac{2P_\perp^2}{\hbar^2}\left(\frac{1}{2E_v} + \frac{\sin^2\xi}{2(E_v - E_{c''})} + \frac{\cos^2\xi}{2(E_v - E_c)}\right). \end{aligned}$$

It is interesting to note that $m_{h\|}$ ($m_{h\perp}$) depends on the interaction with the conduction bands via the Kane parameter $P_\|$ ($P_\perp$). Similarly, the effective masses of the conduction band along and perpendicular to the C-axis are

$$\begin{aligned} \frac{1}{m_{e\|}} &= \frac{1}{m} + \frac{2}{\hbar^2}(L_2\sin^2\xi + M_2\cos^2\xi) + \frac{2P_\|^2}{\hbar^2}\frac{\sin^2\xi}{E_c - E_v}, \\ \frac{1}{m_{e\perp}} &= \frac{1}{m} + \frac{2}{\hbar^2}\left(\frac{L_1 + M_1}{2}\cos^2\xi + M_3\sin^2\xi\right) + \frac{P_\perp^2}{\hbar^2}\frac{\cos^2\xi}{E_c - E_v}, \end{aligned}$$

which are influenced by the interaction with the valence band, as well as by the symmetric parameters L_i and M_i, stemming from the interaction with far bands. The anisotropic effective masses for the valence and conduction bands have been extensively calculated by several first-principles approaches[16,17]. One of the most accurate values are given in ref. 17, which are also consistent with recent cyclotron resonance measurements[23], $m_{h\|} = 0.21\,m$, $m_{h\perp} = 0.23\,m$, $m_{e\|} = 0.15\,m$, and $m_{e\perp} = 0.21\,m$. From these effective masses, we obtain the Kane parameters, $P_\| = 7.64$ eV Å and $P_\perp = 6.95$ eV Å, as well as the symmetric parameters $mL_i/\hbar^2 = -25.90$ and $mM_i/\hbar^2 = 23.39$.

A free electron possesses a magnetic moment of its spin and has a g-factor of $g_0 = 2.0023$. The SOC enables the electron orbital motion to contribute to the magnetic moment and, consequently, the effective g-factor deviates from g_0. In Eq. (9), the g-factors of the valence-band edge along and perpendicular to the C-axis are

$$g_{h\|} = g_0 + 2mP_\perp^2\left(\frac{\cos^2\xi}{E_v - E_c} + \frac{\sin^2\xi}{E_v - E_{c''}} - \frac{1}{E_v}\right), \tag{11}$$

$$g_{h\perp} = g_0 + 2m\sqrt{2}\,\sin\xi\cos\xi P_\| P_\perp\left(\frac{1}{E_v - E_c} - \frac{1}{E_v - E_{c''}}\right). \tag{12}$$

We see that the g-factors depend on the energies of conduction-band edges as well as the Kane parameters. In contrast to the effective mass, $g_{h\|}$ is connected to the conduction bands only via $P_\perp$. This is understandable because a magnetic field $\boldsymbol{B}$ affects the electron orbital motion perpendicular to the field. For the same reason, $g_{h\perp}$ is connected to the conduction bands via both $P_\|$ and $P_\perp$. Using the values of $P_\|$ and $P_\perp$, we obtain the $g_{h\|} = -0.472$ and $g_{h\perp} = -0.354$, which are similar to the value in 2H-PbI_2, $g_h = -0.4$[32]. The negative g-factor means that the up spin has a lower energy than the down spin.

The conduction-band g-factors along and perpendicular to the C-axis are

$$g_{e\|} = 2[-(3\kappa_1 + 2)\cos^2\xi + \sin^2\xi] + 2mP_\perp^2\frac{\cos^2\xi}{E_c - E_v}, \tag{13}$$

$$g_{e\perp} = 2[-(3\kappa_2 + 1)\sqrt{2}\,\sin\xi\cos\xi - \sin^2\xi] + \frac{2\sqrt{2}\,mP_\perp P_\|\sin\xi\cos\xi}{E_c - E_v}, \tag{14}$$

which depend on the antisymmetric Luttinger parameters κ_1 and κ_2, in addition to the $P_{\|(\perp)}$. Thus the values of $g_{e\|}$ and $g_{e\perp}$ can be used to determine κ_1 and κ_2. Experimentally, the exciton g-factor are measured from the energy splitting between left- and right-circularly polarized absorption[33,34] and PL[11], which, as we will discuss below, is

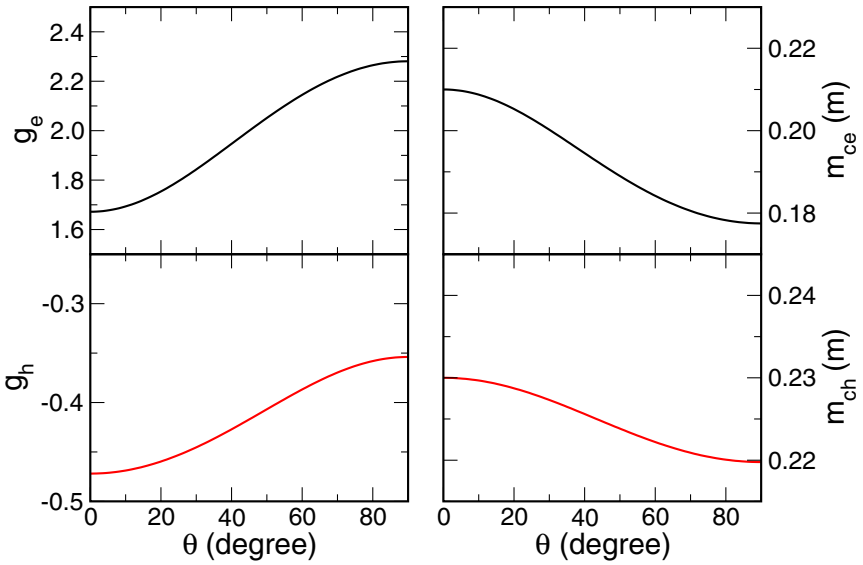

Figure 2. *g*-factors and cyclotron masses of conduction and valence bands. Left panels describe the electron (g_e) and hole (g_h) *g*-factors as a function of angle θ between the C-axis and the applied magnetic field. Right panels describe the electron (m_{ce}) and hole (m_{ch}) cyclotron masses.

$g_{e\|}+g_{h\|}$. If we use $g_{e\|}+g_{h\|}=1.2$, as in ref. 33, we find $g_{e\|}=1.672$ and $\kappa_1=0.269$. If we further assume $\kappa_2=\kappa_1$, we have $g_{e\perp}=2.281$. These values are also similar to those of electrons in 2H-PbI_2, $g_{e\|}=1.4$ and $g_{e\perp}=2.4$[32].

Since both the *g*-factors and the effective masses are anisotropic, the effective spin splitting and the cyclotron frequency depend on the angle θ between the magnetic field and the C-axis,

$$g_{e(h)}(\theta)=(g^2_{e(h)\|}\cos^2\theta+g^2_{e(h)\perp}\sin^2\theta)^{1/2},\ \widetilde{\omega}_{ce(h)}(\theta)=\frac{eB}{m_{e(h)\perp}c}\left(\cos^2\theta+\frac{m_{e(h)\perp}}{m_{e(h)\|}}\sin^2\theta\right)^{1/2}. \quad (15)$$

The derivations can be found in the Methods section. We plot in Fig. 2 the *g*-factors and the effective cyclotron mass, $m_{ce(h)}(\theta)\equiv eB/c\widetilde{\omega}_{ce(h)}(\theta)$ as a function of θ. At $\theta=0$, $g_{e(h)}(\theta)=g_{e(h)\|}$ and $m_{ce(h)}(\theta)=m_{e(h)\perp}$. At $\theta=\pi/2$, $g_{e(h)}(\theta)=g_{e(h)\perp}$ and $m_{ce(h)}(\theta)=\sqrt{m_{e(h)\|}m_{e(h)\perp}}$.

Rashba splitting. The Rashba term, $E_{c(v)r}(k)=\alpha_{c(v)r}(k_y\sigma_x-k_x\sigma_y)$ in Eqs (9) and (10), destroys the spin degeneracy, giving rise to energy-momentum dispersions, $E_c(\boldsymbol{k})=\widetilde{E}_c+\frac{\hbar^2k_\perp^2}{2m_{e\perp}}+\frac{\hbar^2k_z^2}{2m_{e\|}}\pm|\alpha_{cr}|k_\perp$ for the conduction band and $E_v(\boldsymbol{k})=\widetilde{E}_v-\frac{\hbar^2k_\perp^2}{2m_{h\perp}}-\frac{\hbar^2k_z^2}{2m_{h\|}}\pm|\alpha_{vr}|k_\perp$ for the valence band, as plotted in Fig. 3.

The Rashba strengths $\alpha_{c(v)r}$ are directly related to the C_{4v} potential ζ-parameter that characterizes the inversion asymmetry of the structure,

$$\alpha_{vr}=\sqrt{2}\zeta\cos\xi\sin\xi\left(\frac{1}{E_v-E_{c''}}-\frac{1}{E_v-E_c}\right)P_\perp, \quad (16)$$

$$\alpha_{cr}=\sqrt{2}\zeta\cos\xi\sin\xi\frac{1}{E_c-E_v}P_\perp, \quad (17)$$

which indicate that the Rashba splittings in the valence and conduction bands are correlated. Currently the Rashba splittings obtained from different first-principles calculations vary significantly and direct measurements, such as spin-polarized photoemission and spin-flip Raman scattering, of $CH_3NH_3PbI_3$ are not yet available. For $\zeta=0.5$ eV, we have $\alpha_{vr}=0.565$ and $\alpha_{cr}=1.088$ eVÅ.

Exciton wavefunctions. Hybrid perovskite $CH_3NH_3PbI_3$ has a large dielectric constant ε, and the excitons are of the Wannier type, whose wave functions can be written as[35]

$$\psi_{ex}(\boldsymbol{r}_e,\boldsymbol{r}_h)=\sum_{j_e,j_h}c_{j_e}(\boldsymbol{r}_e)\Phi_{j_e,j_h}(\boldsymbol{r}_e-\boldsymbol{r}_h)\bar{v}_{j_h}(\boldsymbol{r}_h) \quad (18)$$

where $j_e,j_h=\pm,\bar{v}_\pm=\hat{\theta}v_\mp$ with $\hat{\theta}$ being the time-reversal operator. $\Phi_{j_e,j_h}(\boldsymbol{r}_e-\boldsymbol{r}_h)$ is the envelop function describing the relative motion of electron and hole and may have *S*, *P*, or *D* characteristics in low magnetic fields, which gradually transforms to that of Landau wave functions with increase of magnetic field.

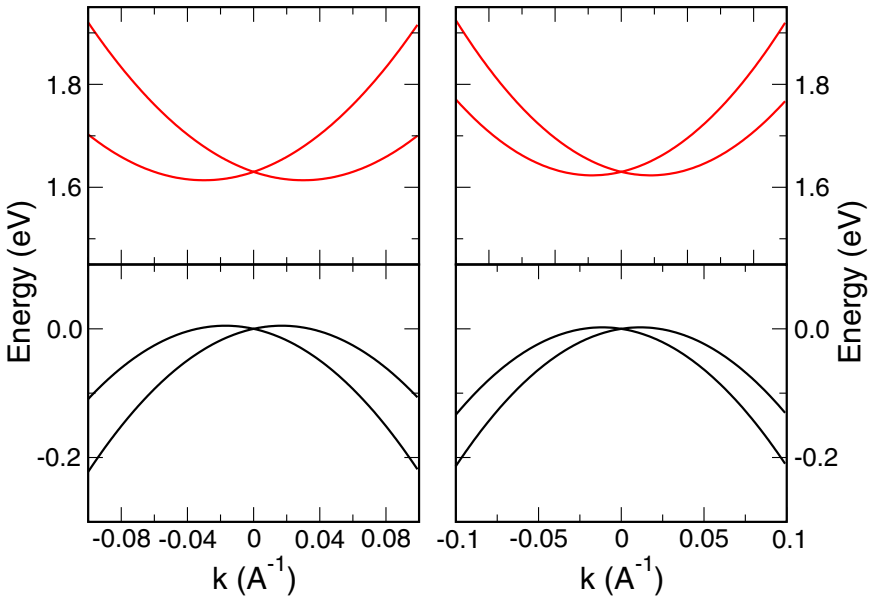

Figure 3. Rashba effect in the conduction and valence bands near the *R* point. Left (right) panel is for $\boldsymbol{k}$ along the [0, 1, 1] ([0, 1, 1]) direction. $\zeta = 0.5$ eV.

The hole (electron) state $\bar{v}_{j_h}$ (c_{j_e}) follows the Γ_6^+ (Γ_6^-) representation of C_{4v}. With $\Phi_{j_e j_h}(\boldsymbol{r}_e - \boldsymbol{r}_h)$ being the 1*S* state, the exciton wavefuctions can be characterized by the C_{4v} representations, $\Gamma_6^+ \otimes \Gamma_6^- = \Gamma_1^- \oplus \Gamma_2^- \oplus \Gamma_5^-$,

$$\begin{aligned}
\psi_1 &= \frac{1}{\sqrt{2}}(c_+\bar{v}_- - c_-\bar{v}_+) = -\frac{1}{2}\cos\xi(X+iY)S\downarrow_e\downarrow_h \\
&\quad + \frac{1}{2}\cos\xi(X-iY)S\uparrow_e\uparrow_h - \frac{1}{2}\sin\xi ZS(\uparrow_e\downarrow_h + \downarrow_e\uparrow_h), \\
\psi_2 &= \frac{1}{\sqrt{2}}(c_+\bar{v}_- + c_-\bar{v}_+) = -\frac{1}{2}\cos\xi(X+iY)S\downarrow_e\downarrow_h \\
&\quad - \frac{1}{2}\cos\xi(X-iY)S\uparrow_e\uparrow_h - \frac{1}{2}\sin\xi ZS(\uparrow_e\downarrow_h - \downarrow_e\uparrow_h), \\
\psi_5^+ &= c_+\bar{v}_+ = -\frac{1}{\sqrt{2}}\cos\xi(X+iY)S\downarrow_e\uparrow_h - \sin\xi ZS\uparrow_e\uparrow_h, \\
\psi_5^- &= c_-\bar{v}_- = -\frac{1}{\sqrt{2}}\cos\xi(X-iY)S\uparrow_e\downarrow_h + \sin\xi ZS\downarrow_e\downarrow_h.
\end{aligned}$$

The total angular momentum $\boldsymbol{J} = \boldsymbol{j}_e + \boldsymbol{j}_h$ is $J = 0$ for ψ_1, $(J, J_z) = (1, 0)$ for ψ_2, and $(J, J_z = 1, \pm 1)$ for $\psi_5^\pm$. The absorption and emission of these states are proportional to the modular square of their electric-dipole elements,

$$\begin{aligned}
\langle\psi_1|\boldsymbol{e}\cdot\boldsymbol{p}|0\rangle &= 0,\ \langle\psi_2|\boldsymbol{e}\cdot\boldsymbol{p}|0\rangle = i\sqrt{2}\sin\xi e_z P_\parallel,\ \langle\psi_5^+|\boldsymbol{e}\cdot\boldsymbol{p}|0\rangle \\
&= -i\cos\xi e_- P_\perp,\ \langle\psi_5^-|\boldsymbol{e}\cdot\boldsymbol{p}|0\rangle = i\cos\xi e_+ P_\perp
\end{aligned}$$

with $e_\pm = \frac{1}{\sqrt{2}}(e_x \pm ie_y)$. Hence ψ_2 can absorb and emit light polarized along the *z*-axis, and $\psi_5^\pm$ can absorb and emit light circularly polarized in the *x*-*y* plane. ψ_1, however, is dark, for it contains only spin triplets and is therefore dipole-forbidden.

The above selection rules in the hybrid perovskites is in stark contrast to those in π-conjugated organic materials with weak SOCs[36], where the electron (hole) has zero angular momentum ($l_z = 0$ for π orbitals) and $J = 1$ is dipole forbidden whereas $J = 0$ is dipole allowed. As we will see below, this difference gives rise to a far richer physics of MFE in the hybrid perovskites.

Paramagnetic effects on excitons. The four 1*S* exciton states, ψ_1, ψ_2, and $\psi_5^\pm$, in general, are not degenerate in energy because of possible exchange interaction between spins $H_{ex} = J_\parallel\sigma_z^e\sigma_z^h + J_\perp(\sigma_x^e\sigma_x^h + \sigma_y^e\sigma_y^h)$, where $\boldsymbol{\sigma}^e/2 = \boldsymbol{j}_e$ and $\boldsymbol{\sigma}^h/2 = \boldsymbol{s}_h$. Consequently the energies of these excitons $E_1 = -J_\parallel - 2J_\perp$, $E_2 = -J_\parallel + 2J_\perp$, $E_5 = J_\parallel$.

An applied magnetic field can modify the exciton energy via the Zeeman energy,

$$H = H_{ex} + H_Z = H_{ex} + \frac{1}{2}\mu_B[g_{e\parallel}\sigma_z^e B_z + g_{e\perp}(\sigma_x^e B_x + \sigma_y^e B_y) + g_{h\parallel}\sigma_z^h B_z + g_{h\perp}(\sigma_x^h B_x + \sigma_y^h B_y)]. \quad (19)$$

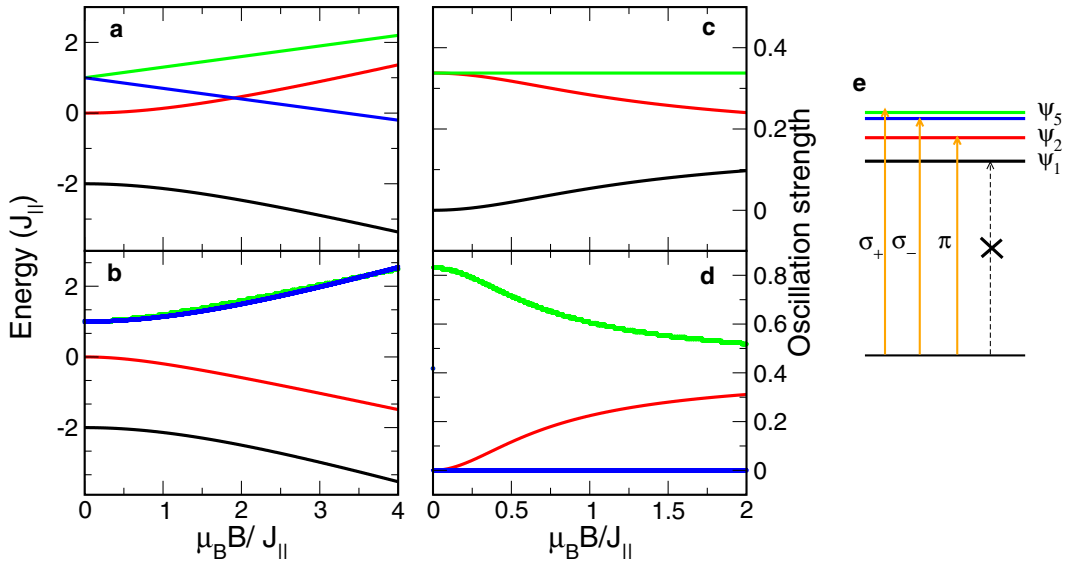

Figure 4. Exciton energies and oscillator strengths vs magnetic field. Panels (a,b) delineate exciton energies as a function of magnetic field in the Faraday and Voigt configurations, respectively. Panels (c,d) are the oscillator strengths of these exciton states along the *z*-axis and the *x*-axis, respectively. Panel (e) illustrates the electric-dipole selection rule of the exciton states. Black and red lines correspond to ψ_1 and ψ_2 excitons. Green and blue lines correspond to ψ_5^+ and ψ_5^- excitons in (**a**,**c**), and ψ_{5L} and ψ_{5T} in (**c**,**d**). Green and blue lines in (**c**) as well as black and blue lines in (**d**) are on top of each other. $J_\parallel = 2J_\perp$.

It should be noted that from the time reversal symmetry, the hole's *g*-factor, including the sign, is identical to that of the valence electron. Since we are concerned with relatively weak magnetic field, we temporarily neglect the diamagnetic effect, which is proportional to B^2 and shift states equally in energy.

In the Faraday configuration with $\boldsymbol{B}$ along the C-axis, $\boldsymbol{B} = (0, 0, B)$, $\psi_5^\pm$ will split in energy, $E_{5\pm} = J_\parallel \pm \frac{1}{2}(g_{e\parallel} + g_{h\parallel})\mu_B B$, and the splitting in absorption and luminescence peaks of left- and right-circularly polarized light, would be $(g_{e\parallel} + g_{h\parallel})\mu_B B$[11,33,34].

The magnetic field $\boldsymbol{B}$ will also mix ψ_1 and ψ_2, with

$$H_1 = \begin{pmatrix} E_1 & (g_{e\parallel} - g_{h\parallel})\mu_B B/2 \\ (g_{e\parallel} - g_{h\parallel})\mu_B B/2 & E_2 \end{pmatrix}. \tag{20}$$

and the energies of eigenstates become $E_{1,2}(B) = -J_\parallel \pm \frac{1}{2}\sqrt{16J_\perp^2 + (g_{e\parallel} - g_{h\parallel})^2\mu_B^2 B^2}$ and their wave functions are $\widetilde{\psi}_i = b_{i1}\psi_1 + b_{i2}\psi_2$ $(i = 1, 2)$. Hence, with increase of the magnetic field, $\widetilde{\psi}_1$ will gain oscillator strength, $|\langle\widetilde{\psi}_1|e_z p_z|0\rangle|^2 \propto |b_{12}|^2$, and flare up, while $\widetilde{\psi}_2$ will lose oscillator strength, $\left|\langle\widetilde{\psi}_2|e_z p_z|0\rangle\right|^2 \propto |b_{22}|^2$, as illustrated in Fig. 4.

In the Vogit configuration with $\boldsymbol{B}$ perpendicular to the C-axis, $\boldsymbol{B} = (B, 0, 0)$, we can construct transverse and longitudinal states out of $\psi_5^\pm$ states, $\psi_{5T} = \frac{1}{\sqrt{2}}(c_+\overline{v}_+ + c_-\overline{v}_-)$ and $\psi_{5L} = \frac{1}{\sqrt{2}}(c_+\overline{v}_+ - c_-\overline{v}_-)$, which have polarization along the *y* and *x* axis, respectively. It is readily to verify that in this configuration, pair (ψ_1, ψ_{5L}) as well as pair (ψ_2, ψ_{5T}) are coupled via the magnetic field, with

$$H_2 = \begin{pmatrix} E_1 & (g_{h\perp} - g_{e\perp})\mu_B B/2 \\ (g_{h\perp} - g_{e\perp})\mu_B B/2 & E_5 \end{pmatrix}, \tag{21}$$

$$H_3 = \begin{pmatrix} E_2 & (g_{e\perp} + g_{h\perp})\mu_B B/2 \\ (g_{e\perp} + g_{h\perp})\mu_B B/2 & E_5 \end{pmatrix}. \tag{22}$$

and their energies are $E_{1,5L}(B) = -J_\perp \pm \frac{1}{2}\sqrt{4(J_\parallel + J_\perp)^2 + (g_{e\perp} - g_{h\perp})^2\mu_B^2 B^2}$ and $E_{2,5T}(B) = J_\perp \pm \frac{1}{2}\sqrt{4(J_\parallel - J_\perp)^2 + (g_{e\perp} + g_{h\perp})^2\mu_B^2 B^2}$. Figure 4 also plots the exciton energies E_1, E_2, E_{5L}, and E_{5T}, as well as their corresponding oscillator strengths $|\langle e_x p_x\rangle|^2$ as a function of the magnetic field.

Magnetic-field effect on photoluminescence. The PL intensity in $CH_3NH_3PbI_3$ is found to be susceptible to a magnetic field at low temperatures[11]. In the Faraday configuration, the magnetic field couples ψ_1 and ψ_2 excitons. Since only the recombination of ψ_2 can give rise to luminescence, the magnetic-field-induced change in

populations of ψ_2 and ψ_1 would lead to an MFE. We employ the Bloch equation of the density matrix to systematically describe the population dynamics,

$$\frac{\partial\hat{\rho}}{\partial t} = \frac{i}{\hbar}[\rho, H_1] + \left(\frac{\partial\hat{\rho}}{\partial t}\right)_g - \frac{\hat{\rho}}{\tau}, \tag{23}$$

where $\hat{\rho}$ is a 2×2 density matrix spanned by ψ_1 and ψ_2, $\hat{\rho} = \sum_{m,n}\rho_{mn}|\psi_m\rangle\langle\psi_n|$ with $m, n = 1, 2$. $(\partial\rho/\partial t)_g$ represents the generation of the exciton states, which is finite only for diagonal terms, $(\partial\rho_{mn}/\partial t)_g = F_m\delta_{mn}$, because the PL in the MFET measurements[11,12] is not resonantly excited. τ is the relaxation time of these exciton states, which includes both recombination τ_l^{-1} and spin relaxation τ_s^{-1}, $\tau^{-1} = \tau_l^{-1} + \tau_s^{-1} \simeq \tau_s^{-1}$, for $\tau_l > 10^{-6}s \gg \tau_s \sim 10^{-10}s$[5,6,11]. In the steady state, $\partial\hat{\rho}/\partial t = 0$, the densities at ψ_1 and ψ_2 can be written as $\rho_{11} = i\tau\Delta g_{\|}Bx/2 + \tau F_1$ and $\rho_{22} = -i\tau\Delta g_{\|}Bx/2 + \tau F_2$, where $\Delta g_{\|} = g_{e\|} - g_{h\|}$ and $x \equiv \rho_{12} - \rho_{21} = i\Delta gB\tau^2(F_1 - F_2)/\{1 + [(\Delta g\mu_B B)^2 + 16J_\perp^2]\tau^2\}$. The intensity change in PL is due to the change in ρ_{22},

$$\Delta I_1 \propto \frac{(\Delta g_{\|}\mu_B B)^2\tau^2}{1 + \left[(\Delta g_{\|}\mu_B B)^2 + 16J_\perp^2\right]\tau^2}. \tag{24}$$

When the exchange is significant with $4J_\perp\tau \gg 1$, $\Delta I_1 \propto B^2/(1 + (B/\overline{B})^2)$ with $\overline{B} = 4J_\perp/\Delta g_{\|}\mu_B$. In this regime, the MFE is suppressed because the magnetic field cannot overcome the exchange to effectively alter the populations on the exciton states for $H < 1$T. When $4J_\perp\tau \ll 1$, the denominator in Eq. (24) becomes $[1 + (\Delta g_{\|}\mu_B B)^2\tau^2]^{-1}$, which represents the so called Δg mechanism of MFE. The Δg mechanism has been found responsible for many MFE phenomena involving radical pairs in organic systems[24]. If the $\Delta g_{\|}$ is known, the Lorentz line shape in Eq. (24) can be used to measure the exciton relaxation time τ, or equivalently, its spin relaxation time.

In the Vogit configuration, the MFE in PL is also expected because the magnetic field, as shown in Eqs (21) and (22), mixes the dark ψ_1 with the dipole-allowed ψ_{5L}, and ψ_2 with ψ_{5T}, which have different oscillator strengths and polarizations, $\sim P_{\|}^2\sin^2\xi/4$ and along the z-axis and $\sim P_\perp^2\cos^2\xi/2$ and along the y-axis for ψ_{5T}, respectively. Using the Bloch equation, we express the PL change in the ψ_1 and ψ_{5L} manifold as

$$\Delta I_2 \propto \frac{(\Delta g_\perp\mu_B B)^2\tau^2}{1 + \left[(\Delta g_\perp\mu_B B)^2 + 4(J_{\|} + J_\perp)^2\right]\tau^2}, \tag{25}$$

where $\Delta g_\perp = g_{e\perp} - g_{h\perp}$, and the PL change in the manifold of ψ_2 and ψ_{5T} as

$$\Delta I_3 \propto \frac{(\Sigma g_\perp\mu_B B)^2\tau^2}{1 + \left[(\Sigma g_\perp\mu_B B)^2 + 4(J_{\|} - J_\perp)^2\right]\tau^2}, \tag{26}$$

where $\Sigma g_\perp = g_{e\perp} + g_{h\perp}$. The MFE in the ψ_1 and ψ_{5L} manifold, ΔI_2, depends on the difference in the g-factors along the x-axis, the direction of the magnetic field, in a very similar fashion as ΔI_1.

The MFE in the ψ_2 and ψ_{5T} manifold, ΔI_3, however, depends on the summation of the electron and hole g-factors along the x-axis. Thus in addition to the Δg mechanism, a Σg mechanism is taking effect in the hybrid perovskites. In the former, the magnetic field modulates the populations between states $J = 0$ and $(J, J_{z(x)}) = (1, 0)$, which can be visualized as the electron and hole spins precess along the magnetic field in the *opposite* directions. In the latter, the magnetic field modulates populations between $(J, J_z) = (1, 0)$ and $(1, \pm 1)$, which can be visualized as the electron and hole spins precess along a transverse magnetic field in the *same* direction. The Σg mechanism is particularly important if the exchange is approximately isotropic, $J_{\|} \simeq J_\perp$, where the $J = 1$ triplet states are degenerate in energy, and according Eq. (26), ΔI_3 is then completely determined by the exciton relaxation time τ, whereas ΔI_1 and ΔI_2 in Eqs (24) and (25) are suppressed by the exchange splitting $4J_\perp$ between the singlet and triplet. For polycrystalline materials, the intensity change should be the combination of the three processes, ΔI_i $(i = 1, 2, 3)$, suggesting that multiple Lorentzen functions may be required to describe experimental data, as shown experimentally[11].

Photoexcitation intensity dependence of MFE. It is observed that the MFE in PL in $CH_3NH_3PbI_3$ is also dependent on the photoexcitation intensity[12]. Only when the intensity reaches a certain threshold, does the MFE become significant. The line shape of MFE shrinks with the increase of the photoexcitation intensity and is eventually stabilized. To explain this unusual intensity dependence, we notice that the MFE, as shown in Fig. 5, is pronounced only when the Zeeman energy dominates over the exchange splitting. As a specific example, we consider the Faraday configuration, where the energy splitting between ψ_1 and ψ_2 is $4J_\perp$. This exchange is of short-range and related to the exciton envelop function $\Phi(\boldsymbol{r})$ at $r = 0$, i.e., when the electron and hole are at the same location. For the $1S$ state,

$$J_\perp \propto |\Phi(r = 0)|^2 = 2/a_0^3, \tag{27}$$

where a_0 is the effective Bohr radius of the exciton, $a_0 = \hbar^2\varepsilon/e^2\mu$ with $\mu^{-1} = m_e^{-1} + m_h^{-1}$ being the effective mass of exciton.

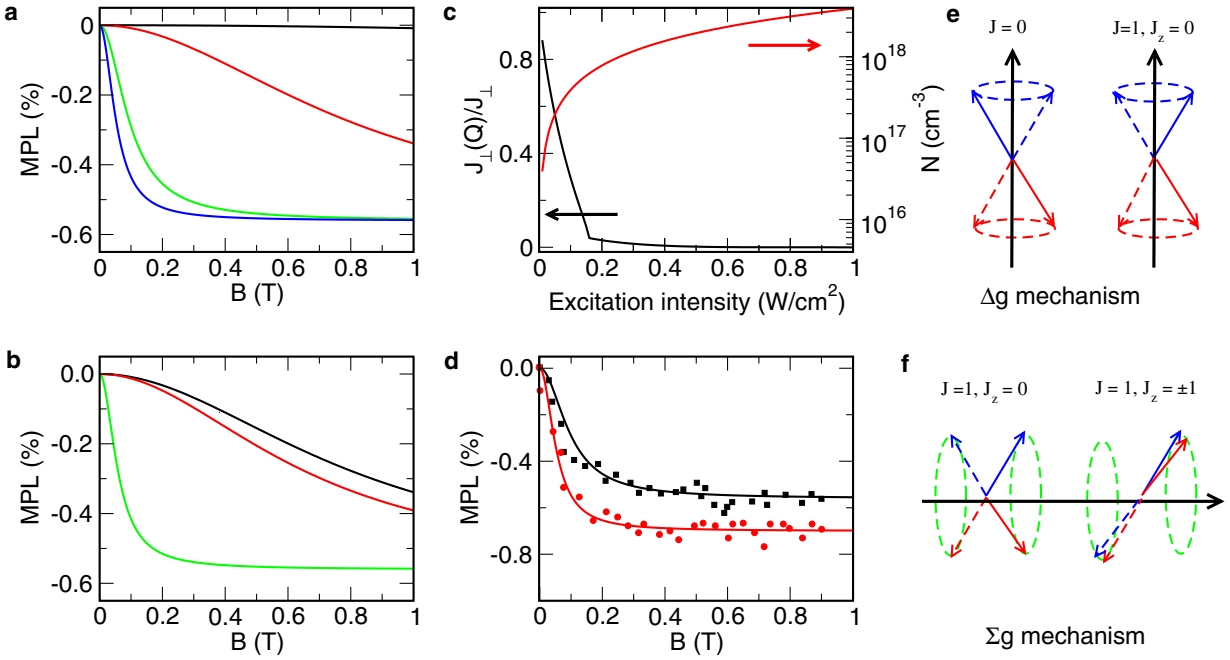

Figure 5. Magnetic field effect in exciton photoluminescence. Panel (a) describes ΔI_1 for exchange splitting between ψ_2 and ψ_1 being $4J_\perp = 1$ (black line), 0.1 (red line), 0.01 (green line), and 0.001(blue line) meV. Panel (b) describes ΔI_1 (black line), ΔI_2 (red line), and ΔI_3 (green line) for $J_\parallel = J_\perp = 0.025$ meV. Panel (c) describes the carrier density and the reduction of the exchange as a function of the intensity of excitation light. Panel (d) plots ΔI_1 as a function of magnetic field with $4J_\perp = 1$ meV for intensities of 0.34 (black line) and 0.85 W/cm^2 (red line). Black and red dots are the corresponding experimental values in ref. 12. Panels (e,f) illustrate the Δg and Σg mechanisms. The exciton relaxation time is fixed at 10^{-10} s.

A high-intensity photoexcitation creates many free electron-hole pairs, whose density can be estimated as $N = \alpha I \tau_l/\hbar\omega$, where α is the absorption coefficient, $\alpha \sim 10^5\,\mathrm{cm}^{-1}$[5] for the $CH_3NH_3PbI_3$, τ_l is the carrier recombination lifetime, $\tau_l \sim 10^{-5}$ s, and $\hbar\omega$ is the photon energy. These free electron-hole pairs will screen the Coulomb interaction, which can be modeled by the Debye-Hückel theory of ion gases[37]. The Coulomb potential $-e^2/\varepsilon r$, in the presence of charged particles, is replaced by the potential U that satisfies the Poisson equation, $(\nabla^2 - Q^2)U = 0$ with $Q^2 = 8\pi e^2/k_B TN$. The solution $U(r)$ is of the Yukawa type $U(r) = -e^2 e^{-Qr}/(\varepsilon r)$, and the ground-state wave function in such a potential can be written as $\widetilde{\Phi}(r) = 2(\beta Q)^{3/2} e^{-\beta Q r}$, where the trial parameter β can be obtained by minimizing the ground state energy of Hamiltonian $-\nabla^2/2\mu + U(r)$, $E = (1)/(2)\beta^2 Q^2\hbar^2/\mu - 4\beta^3 e^2/[\varepsilon Q(4\beta^2 + 4\beta + 1)]$. The wave function $\widetilde{\Phi}$(r), as compared to Φ(r), is more spreaded in space, and the exchange will be reduced by a factor

$$J_\perp(Q)/J_\perp = \left|\widetilde{\Phi}(0)/\Phi(0)\right|^2 = (\beta\hbar^2\varepsilon Q/e^2\mu)^3. \tag{28}$$

Figure 5 illustrates the screening effect. We see that as the intensity of photoexcitation increases, the exchange is greatly reduced. The MFE, meanwhile, becomes significant. After the carrier density reaches $10^{18}\,\mathrm{cm}^{-3}$, the exchange is so small that $4J_\perp(Q)\tau \ll 1$, and the line shape in ΔI_1 is independent of exchange, and therefore the photoexcitation intensity.

Diamagnetic effect on excitons. So far we have considered only the 1*S* exciton states and neglected the diamagnetic effect on excitons. The diamagnetic effect originates from the orbital motions of electron and hole, and has been used to directly measure the exciton's binding energy and effective mass[23]. For free electrons and holes, an applied magnetic field can localized their orbital wave function normal to the magnetic field, forming the Landau levels with the magnetic length of $\sqrt{\hbar c/eB}$. Since the anisotropy in effective mass for both electron and hole are relatively small, as shown in Fig. 2, we use isotropic effective masses, $m_e = (m_{e\parallel} m_{e\perp}^2)^{1/3}$, $m_h = (m_{h\parallel} m_{h\perp}^2)^{1/3}$, and $\mu^{-1} = m_e^{-1} + m_h^{-1}$, to study the diamagnetic effect.

The diamagnetic response of excitons is far more complex than that of free electron-hole pairs, but offers more valuable information on excitons as well as constituent electrons and holes. Under a small magnetic field, the Coulomb interaction in an exciton is predominant and the diamagnetic effect can be studied by applying the perturbation theory to the hydrogen-like exciton wavefunctions. Such a perturbation must fail when the magnetic length $\sqrt{\hbar c/eH}$ becomes much smaller than the orbital radius of exciton, $a_0 = \hbar^2\varepsilon/(e^2\mu)$. In this high-magnetic field regime, it is more appropriate to use the Landau levels as the starting point. A ratio,

$\gamma = \hbar\omega_c/2R_y$, between the exciton cyclotron energy $\hbar\omega_c = eB/(\mu c)$ and the exciton binding energy, $R_y = \mu e^4/(2\varepsilon^2\hbar^2)$, can be used to distinguish the weak ($\gamma < 1$) and strong ($\gamma > 1$) magnetic-field regimes.

The Hamiltonian for the envelop function $\Phi(\boldsymbol{r}_e - \boldsymbol{r}_h)$ at $K = 0$ (K being the center-of-mass momentum of exciton) reads

$$H_{\mathrm{D}} = -\frac{1}{2\mu}\nabla^2 - \frac{e^2}{\varepsilon r} - \frac{e}{2c}(m_e^{-1} - m_h^{-1})\boldsymbol{B}\cdot\boldsymbol{L} + \frac{e^2B^2(x^2+y^2)}{8\mu c^2}, \tag{29}$$

where $\boldsymbol{L} = -i\boldsymbol{r}\times\nabla$ is the orbital angular momentum. While this Hamiltonian of exciton is similar as that of hydrogen atom in a magnetic field, the key difference is that the third term contains $m_e^{-1} - m_h^{-1}$, the difference between electron and hole effective masses, which will reduce to μ^{-1} in the hydrogen case.

To reliably solve the Hamiltonian for an arbitrary magnetic field, we employ two different basis sets[38]. In low magnetic fields, by using a_0 (R_y) as the length (energy) scale, $H_{\mathrm{D}} = -\nabla^2 - \frac{2}{r} + \eta\gamma L_z + \frac{1}{6}\gamma^2 r^2(1 - \sqrt{\frac{4\pi}{5}}Y_{20}(\theta,\phi))$, where $\eta = m/m_e - m/m_h$ and Y_{lm} is spherical harmonic function. We choose the basis set as

$$\Phi_{nlm}(\boldsymbol{r}) = \frac{2}{n^2}\sqrt{\frac{(n-l-1)!}{(n+l)!}}e^{-r/n}\left(\frac{2r}{n}\right)^l L_{n-l-1}^{2l+1}\left(\frac{2r}{n}\right)Y_{lm}(\theta,\phi), \tag{30}$$

which are the eigenstates of $H_0 = -\nabla^2 - \frac{2}{r}$ with L_n^k is the generalized Laguerre polynomials.

In high magnetic fields, by using $(\sqrt{6}/\gamma)^{1/2}a_0$ and $\gamma/\sqrt{6}R_y$ as the length and energy scales $H_{\mathrm{D}} = -\nabla^2 + r^2 + \sqrt{6}\eta L_z - \left(\frac{\sqrt{6}}{\gamma}\right)^{1/2}\frac{2}{r} - \left(\frac{4\pi}{5}\right)^{1/2}r^2Y_{20}$, and the eigenfunctions of a spherical harmonic oscillator $H_0 = -\nabla^2 + r^2$

$$\Psi_{nlm}(\mathbf{r}) = N_{nl}e^{-r^2/2}r^l L_n^{l+\frac{1}{2}}(r^2)\,Y_{lm}(\theta,\phi), \tag{31}$$

with $N_{nl} = 2^{1/2}[n!/\Gamma(n+l+\frac{3}{2})]^{1/2}$ are chosen to be another basis set. These basis sets, with correct characteristics of wave functions in the low- and high-field regimes, facilitate an analytical evaluation of the Hamiltonian matrix elements (see the Methods section). Moreover the basis sets are eigenstates of parity and $L_z = m$, which are good quantum numbers of the Hamiltonian. We use large basis sets in both regimes, $n, l \le 20$ for Φ_{nlm} and $n, l \le 29$ for Ψ_{nlm}, and diagonalize the Hamiltonian to obtain the eigenstates. The large basis sets allow us to approach the intermediate $\gamma \sim 1$ from both $\gamma < 1$ and $\gamma > 1$ regimes so that the solutions from both ends are smoothly connected. In the limit of $\gamma \to \infty$, the eigenstates become the the Landau levels of free electron and hole. $E_v(N_h) = E_v^0 - \hbar\omega_{ch}(N_h + 1/2)$ and $E_c(N_e) = E_c^0 + \hbar\omega_{ce}(N_e + 1/2)$. The optical selection rule for the transition from valence- to conduction-band Landau levels is $N_h = N_e = N$, and the absorption peaks are located at $E = E_g + \frac{\hbar eB}{c\mu}\left(N + \frac{1}{2}\right)$, where E_g is the band gap.

In Fig. 6, we compare the theoretical results with recent cyclotron resonance experiment[23], using the effective masses of $m_h = 0.223\,m$ and $m_e = 0.188\,m$, and the binding energy of 16 meV. The agreement between theory and experiment is excellent. In addition, the pronounced absorption peaks above the 2S state, induced by the magnetic field, are very close to the state $3D_{\pm 2}$, whereas the $2P_0$ state, as assigned in ref. 23 for the absorption peak, is almost degenerate in energy with 2S state. Indeed, transitions to exciton states $\psi_5^+ D_{-2}$ and $\psi_5^- D_{+2}$, according to the selection rule, are electric-dipole allowed and the only reason that these the state is dark at zero field is $\Phi(r=0) = 0$, which become finite in large magnetic fields. Thus we believe that the observed excitonic absorption peak is due to the $3D_{\pm 2}$ states. $3D_{\pm 2}$ states are important in that from their energy splitting, $E_{3D_{+2}} - E_{3D_{-2}} = 4\gamma(m_e^{-1} - m_h^{-1})$, we can obtain the difference in the effective masses of electron and hole, which, together with μ measured from the Landau levels of free electron-hole absorption, can completely determine both m_e and m_h. It is noted that the inter-band cyclotron resonance of free electron-hole pairs can measure only μ, not individual m_e and m_h. Thus cyclotron resonance of excitons reveals more information.

Discussion

The hybrid inorganic-organic perovskites have shown great promise in photovoltaic and many other important applications because of their outstanding transport, optical, and magneto-optical properties. To understand these properties, in this paper, we have constructed a reliable and accessible effective-mass model of the hybrid perovskites, which connects effective masses, Rashba splittings, and anisotropic g-factors of conduction and valence bands. Using this effective-mass model, we have elucidated the observed MFE in exciton PL and its dependence on photoexcitations and identified a new Σg mechanism of MFE. We have also calculated the cyclotron resonance of excitons for arbitrarily strong magnetic fields and pointed out that excitonic states such as $3D_{\pm 2}$ provide information on the difference in effective masses of electron and hole.

This effective-mass model is a foundation on which systematic models of electron-phonon coupling, carrier mobility, and other transport properties can be developed. Because of the concise expressions of SOC, Rashba effect, and g-factor, this model also facilitates studies of spin relaxation[39], spin Hall effect[40], and other magneto optical and spintronic phenomena.

Methods

Expressions of H_A, H_B, and H_C. The three 4×4 matrices in Eq. (7) are displayed as

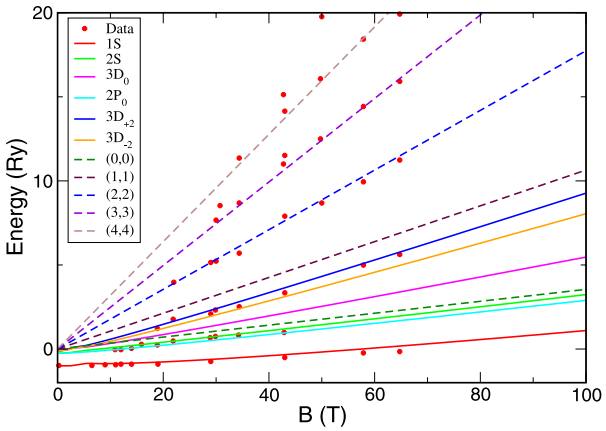

Figure 6. Cyclotron resonance of excitons in $CH_3NH_3PbI_3$. Solid lines are energies of different exciton states. Dashed lines are the energy difference between the Landau levels of free electron and holes with (N, N) being the Landau-level index. Dots are the experimental data from ref. 23. The absorption peak between 2S and (1, 1) coincides with the energies of $3D_{\pm 2}$ states.

$$H_{\mathrm{A}} = \begin{pmatrix} E_v + \frac{eB_z}{2mc} & \frac{eB_-}{2mc} & -\sin\xi(iP_{\parallel}k_z + \zeta) & -i\cos\xi P_{\perp}k_-, \\ & E_v - \frac{eB_z}{2mc} & -i\cos\xi P_{\perp}k_+ & \sin\xi(iP_{\parallel}k_z + \zeta) \\ & & E_c + A_c k_{\perp}^2 + B_c k_z^2 + g_{c\parallel}^0 \frac{eB_z}{4mc} & g_{c\perp}^0 \frac{eB_-}{4mc} \\ & & & E_c + A_c k_{\perp}^2 + B_c k_z^2 - g_{c\parallel}^0 \frac{eB_z}{4mc} \end{pmatrix} \tag{32}$$

where

$$\begin{aligned} A_c &= \frac{L_1 + M_1}{2}\cos^2\xi + M_3\sin^2\xi,\ B_c = L_2\sin^2\xi + M_2\cos^2\xi, \\ g_{c\parallel}^0 &= 2\left(-\frac{3\kappa_1 + 2}{2}\cos^2\xi + \frac{1}{2}\sin^2\xi\right),\ g_{c\perp}^0 = 2\left(-\frac{3\kappa_2 + 1}{\sqrt{2}}\sin\xi\cos\xi - \frac{1}{2}\sin^2\xi\right), \\ k_{\perp}^2 &= k_x^2 + k_y^2,\ k_{\pm} = \frac{1}{\sqrt{2}}(k_x \pm ik_y),\ B_{\pm} = B_x \pm iB_y. \end{aligned}$$

$$H_{\mathrm{B}} = \begin{pmatrix} -iP_{\perp}k_+ & 0 & \cos\xi(iP_{\parallel}k_z + d) & i\sin\xi P_{\perp}k_- \\ 0 & iP_{\parallel}k_- & -i\sin\xi P_{\perp}k_+ & \cos\xi(iP_{\parallel}k_z + d) \\ \sin\xi N_2 k_+ k_z + Z_1\frac{eB_+}{2mc} & U_1\cos\xi & U_2 + Z_2\frac{eB_z}{2mc} & -N_2 k_- k_z + Z_3\frac{eB_-}{2mc} \\ -U_1^*\cos\xi & \sin\xi N_2 k_- k_z - Z_1\frac{eB_-}{2mc} & -N_2 k_+ k_z - Z_3\frac{eB_+}{2mc} & -U_2 + Z_2\frac{eB_z}{2mc} \end{pmatrix} \tag{33}$$

where

$$\begin{aligned} Z_1 &= \frac{1}{2}\cos\xi + \frac{3\kappa_2 + 1}{2\sqrt{2}}\sin\xi, \\ Z_2 &= -\frac{3}{2}(\kappa_1 + 1)\sin\xi\cos\xi, \\ Z_3 &= -\frac{1}{2}\sin\xi\cos\xi + \frac{3\kappa_2 + 1}{2\sqrt{2}}(\sin^2\xi - \cos^2\xi), \\ U_1 &= -\frac{1}{2}\left[(L_1 - M_1)(k_x^2 - k_y^2) - 2iN_1 k_x k_y\right], \\ U_2 &= \sin\xi\cos\xi\left[\left(\frac{L_1 + M_1}{2} - M_3\right)k_{\perp}^2 - (L_2 - M_2)k_z^2\right]. \end{aligned}$$

$$H_C = \begin{pmatrix} A_{c'}k_\perp^2 + B_{c'}k_z^2 - \frac{3}{2}\kappa_1\frac{eB_z}{2mc} & 0 & -\cos\xi N_2 k_- k_z + Z_4\frac{eB_-}{2mc} & U_1 \sin\xi, \\ & A_{c'}k_\perp^2 + B_{c'}k_z^2 + \frac{3}{2}\kappa_1\frac{eB_z}{2mc} & \sin\xi U_1^* & \cos\xi N_2 k_+ k_z + Z_4\frac{eB_+}{2mc}, \\ & & A_{c''}k_\perp^2 + B_{c''}k_z^2 + Z_5\frac{eB_z}{2mc} & Z_6\frac{eB_-}{2mc}, \\ & & & A_{c''}k_\perp^2 + B_{c''}k_z^2 - Z_5\frac{eB_z}{2mc}, \end{pmatrix} \quad (34)$$

where

$$\begin{aligned} A_{c'} &= \frac{L_1 + M_1}{2},\ B_{c'} = M_2 \\ A_{c''} &= \frac{L_1 + M_1}{2}\sin^2\xi + M_3\cos^2\xi,\ B_{c''} = L_2\cos^2\xi + M_2\sin^2\xi \\ Z_4 &= \frac{1}{2}\sin\xi - \frac{3\kappa_2 + 1}{2\sqrt{2}}\cos\xi \\ Z_5 &= \frac{1}{2}\cos^2\xi - \frac{3\kappa_1 + 2}{\sqrt{2}}\sin^2\xi \\ Z_6 &= \frac{1}{2}\cos^2\xi - \frac{3\kappa_2 + 1}{\sqrt{2}}\sin\xi\ \cos\xi. \end{aligned}$$

Derivations of Eq. (15). When the applied magnetic field $\boldsymbol{B}$ tilts away from the crystal C-axis with an angle θ, we can define the new z-axis (denoted z') along $\boldsymbol{B}$ and assume that the tilting is in the x-z plane with the new x-axis denoted as x'. The transformations of coordinates between the two references are

$$\sigma_x' = \cos\theta\sigma_x - \sin\theta\sigma_z,\ \sigma_z' = \sin\theta\sigma_x + \cos\theta\sigma_z,\ \sigma_y' = \sigma_y, \quad (35)$$

$$k_x' = \cos\theta k_x - \sin\theta k_z,\ k_z' = \sin\theta k_x + \cos\theta k_z,\ k_y' = k_y. \quad (36)$$

The Zeeman energy in Eqs (9) and (10) then becomes

$$H_Z = \frac{\mu_B}{2}B\left[(g_\parallel\cos^2\theta + g_\perp\sin^2\theta)\sigma_z' + (g_\perp - g_\parallel)\sigma_x'\ \sin\theta\ \cos\theta\right], \quad (37)$$

and the effective g-factor $g(\theta)$ in Eq. (15) can be obtained by diagnonalizing this Hamiltonian.

In the new reference system, $\left[k_x', k_y'\right] = -ieB/\hbar c$, and the kinetic energy in Eqs (9) and (10) reads

$$E_k = \mathcal{A}k_x'^2 + \mathcal{B}k_y'^2 + \mathcal{C}k_z'^2 + \mathcal{D}k_x'k_z' \quad (38)$$

with $\mathcal{A} = \frac{\hbar^2}{2m_\perp}\cos^2\theta + \frac{\hbar^2}{2m_\parallel}\sin^2\theta$, $\mathcal{B} = \frac{\hbar^2}{2m_\perp}$ $\mathcal{C} = \frac{\hbar^2}{2m_\perp}\sin^2\theta + \frac{\hbar^2}{2m_\parallel}\cos^2\theta$, $\mathcal{D} = \left(\frac{\hbar^2}{2m_\perp} - \frac{\hbar^2}{2m_\parallel}\right)\sin\theta\ \cos\theta$. We can define the ladder operators b and b^+ of the Landau levels as

$$b = \frac{l_B}{\sqrt{2}\,(\mathcal{AB})^{1/4}}\left(\sqrt{\mathcal{A}}k_x' + i\sqrt{\mathcal{B}}k_y' + \frac{\mathcal{D}}{\sqrt{\mathcal{A}}}k_z'\right),\ b^+ = \frac{l_B}{\sqrt{2}\,(\mathcal{AB})^{1/4}}\left(\sqrt{\mathcal{A}}k_x' - i\sqrt{\mathcal{B}}k_y' + \frac{\mathcal{D}}{\sqrt{\mathcal{A}}}k_z'\right), \quad (39)$$

with $l_B = \sqrt{\hbar c/eB}$, which satisfy $[b, b^+] = 1$. The kinetic energy is then expressed as

$$E_k = 2\sqrt{\mathcal{AB}}\frac{eB}{\hbar c}\left(b^+b + \frac{1}{2}\right) + \left(\mathcal{C} - \frac{\mathcal{D}^2}{\mathcal{A}}\right)k_z'^2, \quad (40)$$

with $2\sqrt{\mathcal{AB}} = \frac{\hbar^2}{m_\perp}\left(\cos^2\theta + \frac{m_\perp}{m_\parallel}\sin^2\theta\right)^{1/2}$, which gives $m_c(\theta)$ in Eq. (15).

Matrix elements of H_D in basis sets of Φ_{nlm} and Ψ_{nlm}. The matrix elements of H_D among Φ_{nlm} and among Ψ_{nlm} can be evaluated analytically, which greatly simplifies the eigenstate calculations.

The matrix element of angle-dependent term in the Hamiltonian can be calculated via the integral

$$\int Y_{l_jm_j}^* Y_{20} Y_{l_im_i} d\Omega = (-1)^{m_j}[(2l_i + 1)(2l_j + 1)]^{1/2}\left(\frac{5}{4\pi}\right)^{1/2}\begin{pmatrix} l_j & l_i & 2 \\ 0 & 0 & 0 \end{pmatrix}\begin{pmatrix} l_j & l_i & 2 \\ -m_j & m_i & 0 \end{pmatrix}, \quad (41)$$

where the Wigner 3-j symbols are used.

The only type of matrix elements to be evaluated is r^s between the basis functions. Between basis functions $\Phi_{n_il_im}$ and $\Phi_{n_jl_jm}$,

$$\langle r^s \rangle_{ij} \propto \int_0^\infty r^{l_i+l_j+s+2} e^{-r\left(\frac{1}{n_i}+\frac{1}{n_j}\right)} L_{n_i-l_i-1}^{2l_i+1}\left(\frac{2r}{n_i}\right) L_{n_i-n_j-1}^{2l_j+1}\left(\frac{2r}{n_j}\right) dr. \tag{42}$$

The integral can be worked out analytically,

$$\begin{aligned}\int_0^\infty \Big[\ldots\Big] dr \;=\; & \frac{\Gamma(\gamma)}{\sigma^{\gamma+1}} \sum_{k=0}^{min(m,n)} \binom{m+\alpha}{m-k}\binom{n+\beta}{n-k}\binom{k+\gamma}{k}\left(\frac{\lambda\mu}{\sigma^2}\right)^k \\ & \times {}_2F_1\left(-m+k,\, \gamma+k+1,\, \alpha+k+1;\, \frac{\lambda}{\sigma}\right) \\ & \times {}_2F_1\left(-n+k,\, \gamma+k+1,\, \beta+k+1;\, \frac{\mu}{\sigma}\right)\end{aligned} \tag{43}$$

where $\gamma = l_i + l_j + s + 2$, $\sigma = \frac{1}{n_i} + \frac{1}{n_j}$, $\alpha = 2l_i + 1$, $\beta = 2l_j + 1$, $m = n_i - l_i - 1$, $n = n_j - l_j - 1$, $\lambda = 2/n_j$, $\mu = 2/n_j$, and ${}_2F_1(\alpha, \beta, \gamma; z$ is the Gauss' hypergeometric function.

The matrix element of r^s between basis functions $\Psi_{n_i l_i m}$ and $\Psi_{n_j l_j m}$, neglecting the normalization factor, is

$$\begin{aligned}&\int_0^\infty r^{\frac{l_i+l_j+s+1}{2}} e^{-r} L_{n_i}^{l_i+\frac{1}{2}}(r) L_{n_j}^{l_j+\frac{1}{2}}(r)\, dr \\ &= \Gamma\left(\frac{l_i+l_j+s+3}{2}\right) \sum_{k=0}^{min(n_i,n_j)} \binom{n_i+l_i+\frac{1}{2}}{n_i-k}\binom{n_j+l_j+\frac{1}{2}}{n_j-k} \\ &\quad \times \binom{k+\frac{1}{2}(l_i+l_j+s+1)}{k} {}_2F_1\left(-n_i+k,\, \frac{1}{2}(l_i+l_j+s+3)+k,\, l_i+k+\frac{3}{2};\, 1\right) \\ &\quad \times {}_2F_1\left(-n_j+k,\, \frac{1}{2}(l_i+l_j+s+3)+k,\, l_j+k+\frac{3}{2};\, 1\right).\end{aligned} \tag{44}$$

References

1. Kojima, A., Teshima, K., Shirai, Y. & Miyasaka, T. Organometal halide perovskites as visible-light sensitizers for photovoltaic cells. *J. Am. Chem. Soc.* **131,** 6050 (2009).
2. Etgar, L. *et al.* Mesoscopic $CH_3NH_3PbI_3/TiO_2$ heterojunction solar cells. *J. Am. Chem. Soc.* **134** 17396 (2012).
3. Burschka, J. *et al.* Sequential deposition as a route to high-performance perovskite-sensitized solar cells. *Nature* **499,** 316 (2013).
4. Lee, M. M., Teuscher, J., Miyasaka, T., Murakami, T. N. & Snaith, H. J. Efficient hybrid solar cells based on meso-superstructured organometal halide perovskites. *Science* **338,** 643 (2012).
5. Dong, Q. *et al.* Electron-hole diffusion lengths >175 μm in solution-grown $CH_3NH_3PbI_3$ single crystals. *Science* **347,** 967 (2015).
6. Shi, D. *et al.* Low trap-state density and long carrier diffusion in organolead trihalide perovskite single crystals. *Science* **347,** 519 (2015).
7. Even, J., Pedesseau, L., Jancu, J.-M. & Katan, C. Importance of spin-orbit coupling in hybrid organic/inorganic perovskites for photovoltaic applications. *J. Phys. Chem. Lett.* **4,** 2999 (2013).
8. Jin, H., Im, J. & Freeman, A. J. Topological insulator phase in halide perovskite structures. *Phys. Rev. B* **86,** 121102(R) (2012).
9. Kim, M., Im, J., Freeman, A. J., Ihm, J. & Jin, H. Switchable S = 1/2 and J = 1/2 Rashba bands in ferroelectric halide perovskites. *Proc. Natl. Acad. Sci. USA* **111,** 6900 (2014).
10. Ishihara, T., Takahashi, J. & Goto, T. Optical properties due to electronic transitions in two-dimensional semiconductors $(C_nH_{2n+1}NH_3)_2PbI_4$. *Phys. Rev. B* **42,** 11099 (1990).
11. Zhang, C. *et al.* Magnetic field effects in hybrid perovskite devices. *Nat. Phys.* **11,** 427 (2015).
12. Hsiao, Y. C., Wu, T., Li, M. & Hu, B. Magneto-optical studies on spin-dependent charge recombination and dissociation in perovskite solar cells. *Adv. Mater.* **27,** 2899 (2015).
13. Cho, H. *et al.* Overcoming the electroluminescence efficiency limitations of perovskite light-emitting diodes. *Science* **350,** 1222 (2015).
14. He, Y. & Galli, G. Perovskites for Solar Thermoelectric Applications: A First Principle Study of $CH_3NH_3AI_3$ (A = Pb and Sn). *Chem. Mater.* **26,** 5394 (2014)
15. Even, J., Pedesseau, L., Jancu, J.-M. & Katan, C. DFT and $\boldsymbol{k}\cdot\boldsymbol{p}$ modelling of the phase transitions of lead and tin halide perovskites for photovoltaic cells. *Phys. Status Solidi RRL* **8,** 31 (2014).
16. Brivio, F., Butler, K. T., Walsh, A. & van Schilfgaarde, M. Relativistic quasiparticle self-consistent electronic structure of hybrid halide perovskite photovoltaic absorbers. *Phys. Rev. B* **89,** 155204 (2014).
17. Menéndez-Proupin, E., Palacios, P., Wahnón, P. & Conesa, J. C. Self-consistent relativistic band structure of the $CH_3NH_3PbI_3$ perovskite. *Phys. Rev. B* **90,** 045207 (2014).
18. Luttinger, J. M. & Kohn, W. Motion of Electrons and Holes in Perturbed Periodic Fields. *Phys. Rev.* **97,** 869 (1955)
19. Luttinger, J. M. Quantum theory of cyclotron resonance in semiconductors: General theory. *Phys. Rev.* **102,** 1030 (1956).
20. Kane, E. O. Band Structure of Indium Antimonide. *J. Phys. Chem. Solids* **1,** 249 (1957).
21. D'Innocenzo, V. *et al.* Excitons versus free charges in organo-lead-tri-halide perovskites. *Nat. Commun.* **5,** 3586 (2014).
22. Even, J., Pedesseau, L. & Katan, C. Analysis of multivalley and multibandgap absorption and enhancement of free carriers related to exciton screening in hybrid perovskites. *J. Phys. Chem. C* **118,** 11566 (2014).
23. Miyata, A., Mitioglu, A., Plochocka, P., Portugall, O., Wang, J. T.-W., Stranks, S. D., Snaith, H. J. & Nicholas, R. J. Direct measurement of the exciton binding energy and effective masses for charge carriers in organicÐinorganic tri-halide perovskites. *Nat. Phys.* **11,** 582 (2015).
24. Steiner, U. E. & Ulrich, T. Magnetic field effects in chemical kinetics and related phenomena. *Chem. Rev.* **89,** 51 (1989).
25. Baikie, T. *et al.* Synthesis and crystal chemistry of the hybrid perovskite $(CH_3NH_3)PbI3$ for solid-state sensitised solar cell applications. *J. Mater. Chem. A* **1,** 5628 (2013).

26. Stoumpos, C. C., Malliakas, C. D. & Kanatzidis, M. G. Semiconducting tin and lead Iodide perovskites with organic cations: Phase transitions, high mobilities, and near-infrared photoluminescent properties. *Inorg. Chem.* **52,** 9019 (2013).
27. Schlüter, I. Ch. & Schlüter, M. Electronic structure and optical properties of PbI_2. *Phys. Rev. B* **9,** *1652* (1974).
28. Chuiki, G., Don, N., Dvornik, O., Ivchenko, V. & Sergeyev, A. Simple inverted band structure model for Cadmium Arsenide (Cd_3As_2). *Moldavian J. Phys. Sci.* **2,** 88 (2003).
29. Hirasawa, M., Ishihara, T. & Goto, T. Exciton features in 0-, 2-, and 3-dimensional networks of $[PbI_6]\bar{4}$ octahedra. *J. Phys. Soc. Jpn.* **63,** 3870 (1994).
30. Landau, L. D. & Lifshitz, E. M. *Quantum Mechanics* (Pergamon, Oxford, 1977).
31. Löwdin, P. O. A Note on the quantum-mechanical perturbation theory. *J. Chem. Phys.* **19,** 1396 (1951).
32. Skolnick, M. S. & Bimberg, D. Angular-dependent magnetoluminescence study of the layer compound 2H-PbI_2. *Phys. Rev. B* **18,** 7080 (1978).
33. Hirasawa, M., Ishihara, T., Goto, T., Uchida, K. & Miura, N. Magnetoabsorption of the lowest exciton in perovskite-type compound $CH_3NH_3PbI_3$. *Physica B* **201,** 427 (1994).
34. Tanaka, K. *et al.* Comparative study on the excitons in lead-halide-based perovskite type crystals $CH_3NH_3PbBr_3$ and $CH_3NH_3PbI_3$. *Solid. State Commun.* **127,** 619 (2003).
35. Knox, R. S. *Theory of Excitons* (Academic Press, New York, 1963).
36. Yu, Z. G. Spin-orbit coupling, spin relaxation, and spin diffusion in organic solids. *Phys. Rev. Lett.* **106,** 106602 (2011).
37. Debye, P. & Hückel, E. The theory of electrolytes. I. Lowering of freezing point and related phenomena. *Physikalische Zeitschrift* **24,** 185 (1923).
38. Brandi, H. S. Hydrogen atom in strong magnetic fields. *Phys. Rev. A* **11** 1835 (1975).
39. Giovanni, D. *et al.* Highly spin-polarized carrier dynamics and ultralarge photoinduced magnetization in $CH_3NH_3PbI_3$ perovskite thin films. *Nano Lett.* **15,** 1553 (2015).
40. Yu, Z. G. Spin Hall effect in disordered organic solids. *Phys. Rev. Lett.* **115,** 026601 (2015).

Acknowledgements

I thank B. Hu, Y. Li, D. Sun, and Z. V. Vardeny for useful discussions. This work was partly supported by the US Army Research Office under Contract No. W911NF-15-1-0117.

Author Contributions

Z.G.Y. conceived the concept, performed the calculations, analyzed the results and wrote the manuscript.

Additional Information

Competing financial interests: The author declares no competing financial interests.

How to cite this article: Yu, Z. G. Effective-mass model and magneto-optical properties in hybrid perovskites. *Sci. Rep.* **6**, 28576; doi: 10.1038/srep28576 (2016).